

CONSTRAINTS ON COOL GAS IN RICH CLUSTERS OF GALAXIES

ERIC D. MILLER

Dept. of Astronomy, University of Michigan, Ann Arbor, MI emiller@astro.lsa.umich.edu

JOEL N. BREGMAN

Dept. of Astronomy, University of Michigan, Ann Arbor, MI jbregman@umich.edu

PATRICIA M. KNEZEK

STScI, Baltimore, MD knezek@stsci.edu

Draft version February 1, 2008

ABSTRACT

Cool gas should be present in galaxy clusters due to stripping of galactic gas, infall onto the cluster, and from cooling flows. We searched for this gas through resonance absorption line observations from low-ionization metal line gas toward six background quasars. Both cooling flow and non-cooling flow clusters were observed, with lines of sight from the inner to outer parts of the cluster ($0.2 \leq r_{\text{proj}}/R_{\text{cluster}} \leq 0.7$). The HST/FOS spectra failed to detect Fe II or Mg II absorption at the cluster redshift, with $1\text{-}\sigma$ upper limits on the ion column densities of $N \leq 10^{12}\text{--}10^{13} \text{ cm}^{-2}$. The failure to detect absorption lines implies that the cool cluster gas either is more highly ionized or it has a low covering factor.

1. INTRODUCTION

Rich clusters of galaxies, such as the Abell clusters, are filled with $\sim 10^{14} M_{\odot}$ of hot ($T \sim 10^7$) X-ray emitting gas (see, e.g., Fabian, Nulsen, and Canizares 1991). The density of this gas is largest in the central region ($0.1 - 0.001 \text{ cm}^{-3}$) and decreases with radius, where it becomes undetectable to X-ray instruments when $n_e < 10^{-4} \text{ cm}^{-3}$ (typically at radii of 1 - 3 Mpc; $H_0 = 50 \text{ km s}^{-1} \text{ Mpc}^{-1}$ throughout). Although studies of cluster gas have focused on the hot medium, three important processes can produce cool gas ($T \sim 10^3\text{--}10^4 \text{ K}$) in rich clusters of galaxies: stripping of galactic gas by the hot ambient medium; infall of cool gas into the cluster; and the radiative cooling of the hot gas in the cluster core (cooling flows).

The stripping of galactic gas is expected to be the main process by which the cluster gas becomes enriched, so it is central to interpreting cluster metallicities. The rate at which gas is removed from the ensemble of galaxies is $\sim 100 M_{\odot} \text{ yr}^{-1}$ (Soker, Bregman, and Sarazin 1991), this gas should be near solar metallicity, and the stripping should occur in the inner 1 Mpc of the cluster, where the ambient medium is densest (Gaetz, Salpeter, and Shaviv 1987). The infall of gas onto clusters occurs at the outer regions (3 Mpc radius), it will involve low metallicity material, and the infall rate is expected to be $\sim 10^3 - 10^4 M_{\odot} \text{ yr}^{-1}$. The growth rate of the cluster by infalling gas is a prime growth mechanism for clusters. Finally, in the central 100 kpc, clusters with cooling flows are believed to deposit cooled gas of approximately 1/3 solar metallicity and at the rate of $\sim 100 M_{\odot} \text{ yr}^{-1}$. Each of these mechanisms is distinct both in the spatial distribution for the absorption and in the metallicity of the gas. This paper is the first in an effort to study this cooled gas through the presence of absorption lines.

There have been studies at a variety of wavebands in an effort to detect cool gas. Direct detection of HI in absorption and emission have met with some success, although large quantities of gas are not discovered, and CO emission

remains undetected (McNamara, Bregman, and O'Connell 1990; McNamara and Jaffe 1994; O'Dea, Baum, and Gallimore 1994; O'Dea et al. 1994; O'Dea, Gallimore, and Baum 1995; O'Dea, Payne, and Kocevski 1998). Indirect evidence for cool gas has been obtained by far infrared studies that are sensitive to thermal reemission from dust, where weak emission is seen in a minority of galaxy clusters (Maoz 1995; Cox, Bregman, and Schombert 1995; Stickel et al. 1998). Large amounts of cooled gas ($10^{12} M_{\odot}$) are inferred from the excess soft X-ray absorption toward the central regions (within $r < 0.5 \text{ Mpc}$) of cooling flow clusters (White et al. 1991; Allen et al. 1993; Fabian et al. 1994; Fukazawa et al. 1995), although this result has been questioned (Arabadjis and Bregman 1999).

Cooled material is detectable through UV and optical absorption line studies against background point sources. In a recent study, Koekemoer et al. (1998) searched for absorption against a quasar associated with the central galaxy of Abell 1030. No lines were detected and they obtain $1\text{-}\sigma$ upper limits on the column density for a number of species, including HI ($N < 10^{12.4} \text{ cm}^{-2}$), MgII ($N < 10^{11.5} \text{ cm}^{-2}$), and FeII ($N < 10^{12.0} \text{ cm}^{-2}$). In another study, toward NGC 1275 in Perseus (Johnstone and Fabian 1995), there is a dip in the middle of the Ly α emission line at the velocity of the 21 cm HI absorption feature, which may be interpreted as Ly α absorption with an equivalent width in the 1-5 Å range. However, Johnstone and Fabian (1995) interpret the Ly α emission line as being double but without absorption, which illustrates the difficulty of analyzing emission and absorption features at the same redshift.

The problem with using an AGN in the center of a cluster is that if absorption is detected, it is difficult to distinguish absorption in the AGN from cluster absorption. Alternatively, a failure to detect absorption might be due to the strong photoionizing influence of the AGN on the cool gas. Both problems are avoided by detecting cool ICM gas through absorption against background AGNs which are unrelated to the cluster. This technique has the desirable feature that the cluster and background source

are well separated in velocity space, allowing clean identification of spectral features from each. In addition, the path length covers the entire cluster, thereby maximizing the likelihood of detection. We have obtained near-UV spectra of five background QSOs behind different clusters, supplemented by an additional QSO spectrum from the HST archive. With these six independent lines of sight at various distances from the cluster cores, we have searched for low ionization metal resonance lines.

2. TARGET SELECTION AND OBSERVATIONS

The background AGNs were identified by us as part of a program to find continuum point sources positioned behind galaxies and clusters of galaxies (Knezek and Bregman 1998). Our procedure was to use archived ROSAT X-ray images of nearly sixty northern hemisphere clusters and identify point sources, many of which are background AGNs. We obtained optical spectrophotometry of the sources with the MDM 2.4m telescope, and when AGNs were confirmed through their emission line spectra, we determined their redshifts, fluxes and spectral shapes.

The confirmed AGNs were screened by brightness, redshift, reddening, and projected distance from the cluster center, and the best targets were chosen for observation with HST. In particular, to allow for unambiguous detection of the MgII $\lambda 2800$ doublet, we limited the redshift to $z < 1.3$. At redshifts greater than this, the Ly α forest is shifted past the MgII doublet, which could cause false detections (this is a problem for the sixth target, taken from the archive, as it has $z > 1.3$).

The final sample is unbiased and representative of clusters as a whole, as our selection of AGNs samples a range of projected radii and X-ray properties. Two of the AGNs lie within the inner one-fifth of the cluster radius, while the other four lie between $0.3\text{--}0.72 R_{\text{cluster}}$. With regards to the X-ray properties, one of the clusters, Abell 1795, exhibits a very large cooling rate while Abell 754 has a more modest flow. Two of the clusters, Abell 21 and Coma, show no evidence of cooling flows. The remaining two, Abell 151 and Abell 1267, do not have public X-ray data, although they are nearby and should be bright. Finally, our sample is unbiased by the selection of AGNs, since these background sources are completely uncorrelated to the clusters themselves.

The data for this project were obtained with the Faint Object Spectrograph (FOS). Each spectrum was taken through the $0.86''$ circular aperture using the G270H grating and Red Digicon detector. In this configuration, the spectrum covers the $2222\text{--}3277 \text{ \AA}$ range, and the expected FOS instrumental line width (FWHM) is 2.04 \AA , which produces a spectral resolution of 219 km s^{-1} at 2800 \AA .

The observations are summarized in Table 1, which lists the date and exposure time for each observation, as well as characteristics of each QSO and cluster. Five of the observations were obtained for this program. The sixth, QSO 1258+285 behind the Coma cluster, was obtained from the HST Data Archives to increase our sample. Additional GHRS spectra in the far-UV were also retrieved, but were found to be of poor quality for this project.

Each data set was recalibrated with the CALFOS routine in the IRAF/STSDAS package, using the best reference files available. This produced a substantial improve-

ment (about a factor of 1.5) in the signal-to-noise over the initial pipeline processing. The calibrated spectra along with the propagated photon counting errors are shown in Figure 1; important QSO emission lines are marked.

The identification of absorption lines and measurement of their strengths were performed using the HST Absorption Line Key Project software (Schneider et al. 1993). First, a QSO “continuum” was fit to each spectrum with a series of spline curves. This fit included the QSO emission lines to allow detection of absorption lines superimposed on these features; each spectrum and associated error array was normalized to unity. The line-searching software takes as input parameters the maximum Gaussian width (FWHM), detection limit (defined in terms of the significance level of the measured equivalent width), and the PSF characteristics. The software performs both PSF and Gaussian fitting to the input spectrum, applying multiple Gaussians in the case of blended features. (A detailed description of the line-searching algorithm is provided by Schneider et al. 1993.) We constrained the FWHM of an absorption line to lie between the instrumental limit and that corresponding to a velocity dispersion of 1000 km s^{-1} , which is greater than the velocity dispersion of these clusters. A detection threshold of $3\text{-}\sigma$ was used.

Several lines were detected in each spectrum, and these are listed in Table 2 along with their measured equivalent widths and our identifications. The strong Galactic lines of FeII ($\lambda 2344$, $\lambda 2374$, $\lambda 2382$, $\lambda 2586$, and $\lambda 2600$), MgII ($\lambda \lambda 2796, 2803$), and MgI ($\lambda 2853$) appear in every spectrum, with line strengths ranging from 0.2 \AA for the MgI line to about 1.0 \AA for the stronger line of the MgII doublet (Figure 1; all wavelengths are in vacuum.) Analysis of the Galactic features sheds some light on the quality of the wavelength calibration. The wavelength zeropoint of FOS was not constant between observations, but varied as a result of non-repeatability of the filter/grating wheel position, in addition to other effects. Since contemporaneous wavelength calibration data were not taken with any of the object spectra, the wavelength zeropoint could be displaced by as much as 250 km s^{-1} (Keyes, HST Handbook). Indeed, the line centers of the Galactic lines are shifted from rest by as much as $\pm 2.0 \text{ \AA}$ ($\pm 225 \text{ km s}^{-1}$) in our spectra. Since it is impossible to separate true Galactic motion from errors in the wavelength zeropoint, we have adopted the convention of the HST key project team and have shifted each spectrum so that the Milky Way lines are at rest, using the strong FeII and MgII lines as reference. All figures and data reported in this paper reflect this adjustment.

In addition to the Galactic lines, several other features have been identified in the spectra, and are described below. No sets of lines within $\pm 3000 \text{ km s}^{-1}$ of the cluster redshift were identified for any of the clusters. The spectra in Figure 1 show the regions in which we would expect to see the MgII or FeII absorption produced by cool cluster gas.

To detect fainter absorption features, we searched each spectrum using a detection threshold of $1.5\text{-}\sigma$. Detected lines falling within the expected regions were compared in velocity and line strength to see if they were plausible components of the same species. No satisfactory matches were made.

3. ANALYSIS

3.1. Absorption Systems

We see absorption by several systems which are unrelated to the intervening Abell clusters or to the Galaxy.

QSO 0107–156: We observe a $W_\lambda \approx 1.0$ Å absorption line at 2244.8 Å, superimposed on the QSO Ly α emission line. This could be due to an HI cloud in the AGN itself, in which case the cloud would be outflowing at -1630 km s $^{-1}$ relative to the QSO.

This spectrum contains two additional absorption lines that are more difficult to identify: $W_\lambda = 0.94$ Å at 2397.5 Å and $W_\lambda = 0.63$ Å at 2402.0 Å. In the rest frame of the cluster, these lines would fall at 2277.7 and 2282.0 Å, respectively; in the rest frame of the QSO, they would be 1739.8 and 1743.1 Å. There are no known resonance lines at these wavelengths. If this absorption were due to intervening material, e.g. from FeII λ 2374 or λ 2382, we would expect to see absorption elsewhere in the spectrum from species in a similar ionization state. (In the example, FeII λ 2600 would fall in the range 2615–2630 Å and have $W_\lambda > 0.7$ Å; the 1- σ equivalent width limit, found below, is 0.06 Å in this region of the spectrum.)

The most likely identification for this pair of lines is the C IV doublet at 1548 Å and 1550 Å due to an intervening redshift system at $z = 0.549$. The separation between the pair of absorption lines is 4.5 Å, while the redshifted separation of the C IV doublet is 4.00 Å, a 3.6 σ difference. Also, the ratio of the two lines, $W_{2402}/W_{2397} = 0.67$, is consistent with the ratio from the C IV doublet in the optically thin limit. Unfortunately, we cannot confirm this suggestion by observing other high-ionization lines, since the strong lines lie below the wavelength limit of our observation. The only other line pair with the same fraction separation as the observed absorption lines are the OI λ 1302 and the SiII λ 1304 lines, which would have a redshift of 0.841. However, we rule out this identification due to the absence of other strong low-ionization absorption lines at the same redshift.

QSO 1127+269: We discovered strong FeII and MgII absorption at $z = 0.152$ from a system between this QSO and the foreground cluster. These features are noted by tick marks in Figure 1. Imaging at V and I bands by us with the MDM 1.3m telescope yielded no evidence of faint structure superimposed on or near the QSO.

QSO 1258+285: This spectrum appears to contain several Ly forest lines blueward of the QSO Ly α and Ly β emission lines. It is difficult to identify absorption from the intervening cluster gas against this forest. In particular, the region where we would expect to find MgII absorption lies directly on the Ly α emission from the QSO, making it impossible to separate true absorption from structure in the emission line. There appears to be absorption in some of the regions where we expect to find some of the FeII absorption lines within the cluster. However, one of the strongest Fe lines, FeII λ 2600 is undetected, so we conclude that Fe II absorption at the cluster redshift is unlikely. Absorption at the location of several other Fe II lines are probably Ly forest lines.

Since the QSO Ly β line is shifted into our wavelength region, we can attempt to match corresponding Ly β and Ly α forest lines. For example, the doublet seen at 2280 Å is repeated 2700 Å, making this a likely Ly β /Ly α pair.

Other such pairs are observed at 2320 Å/2750 Å and 2415 Å/2860 Å, the latter of these being strong absorption near or within the QSO. The features seen between 2450–2620 Å could be Ly α forest lines, however their Ly β counterparts would lie below our short-wavelength cutoff. For redshift determination of these and other ambiguous features in Table 2, we assume they are Ly α lines.

3.2. ICM Metal Absorption Limits

We can place an upper limit on the equivalent width of any expected absorption lines simply by using the noise calculations performed by the line-searching software. The upper limits correspond to a maximum velocity dispersion of $\sigma = 1000$ km s $^{-1}$ and are such that these lines, if present, would fall on the linear portion of the curve of growth. The column density for a weak (optically thin) line can be determined in the usual fashion using the relation (see, e.g., Spitzer 1978)

$$N = 1.13 \times 10^{20} W_\lambda(\text{Å}) / f \lambda^2(\text{Å}) \text{ cm}^{-2}$$

After correcting the equivalent width limits for redshift, we found upper limits to the column density of each species with lines falling in our spectral range. We employed a weighted average over all lines of a given species to further constrain the column density, weighting by the expected line strength and then adding individual line contributions in quadrature. The resulting 1-sigma upper limits to the column densities for each cluster are listed in Table 3, along with the wavelength and f -value of the strongest expected transition of each species.

4. CONCLUSIONS

We have placed strict constraints on the amount of low-ionization absorbing material present in rich clusters of galaxies. If we assume a large covering fraction, then the column densities of the species in Table 2 are $N \leq 10^{12} - 10^{13}$ cm $^{-2}$, and there is little low-ionization cool gas in the ICM. Our results are consistent with those of Koekemoer et al. (1998), who found similar limits to N for a variety of species along a single line of sight in Abell 1030.

The results permit us to place constraints on the covering fraction of cool absorbing gas. With six independent lines of sight producing non-detections for the strongest expected line (MgII λ 2796), the covering fraction of low-ionization gas with $N(\text{MgII}) \geq 3 \times 10^{12}$ cm $^{-2}$ must be less than 40%, at the 95% confidence level.

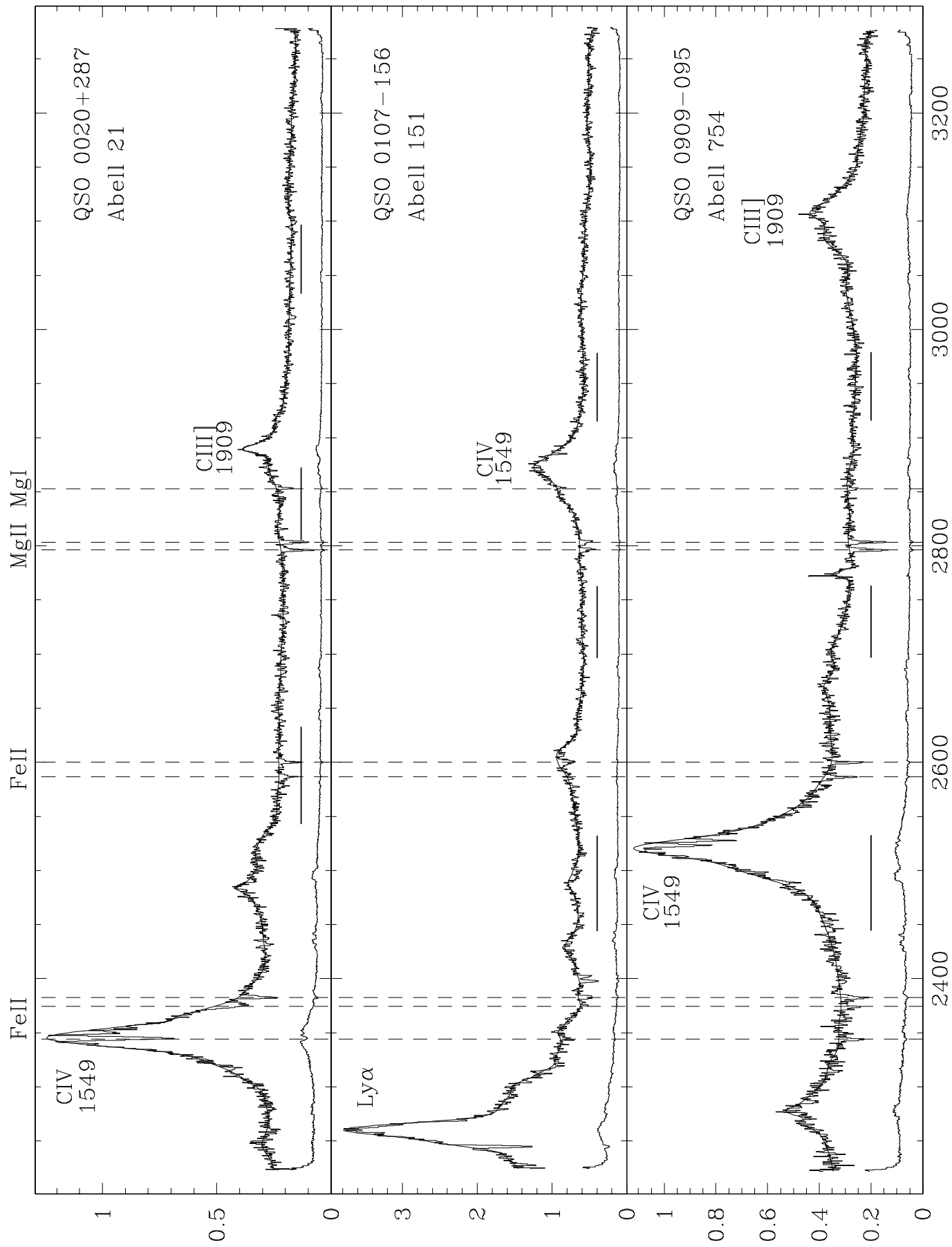
Although low ionization gas does not appear to have a large covering factor in galaxy clusters, little is known about higher ionization state gas, as is often identified through CIV and SiIV absorption. There are expectations that searches with the higher ionization will be more successful, based upon a few observations through other clusters. In an observation toward 3C 273, which lies behind the outer part of the Virgo cluster, Ly α absorption was detected at the redshift of the Virgo cluster (Bahcall et al. 1991). It has a HI column density of at least 4×10^{14} cm $^{-2}$ and has detectable high ionization metal absorption lines (Hurwitz et al. 1998 and references therein). In the future, we hope to study whether clusters are sites of high-ionization absorption lines, and whether they produce Ly α absorption, thus completing the study of the absorbing properties of galaxy clusters.

We would like to thank Don Schneider, Jane Charleton, and Kaspar von Braun for their insights and assistance.

Financial support was provided by NASA through the HST GO program.

REFERENCES

- Allen, S.W., Fabian, A.C., Johnstone, R.M., White, D.A., Daines, S.J., Edge, A.C., Stewart, G.C. 1993, MNRAS, 262, 901
Bahcall, J.N., Jannuzi, B.T., Schneider, D.P., Hartig, G.F., Bohlin, R., and Junkkarinen, V. 1991, ApJ, 377, L5.
Braine, J., Wyrowski, F., Radford, S.J.E., Henkel, C., and Lesch, H. 1995, A&A, 293, 315
Cox, C.V., Bregman, J.N., and Schombert, J.M. 1995, ApJS, 99, 405
Dwek, E., Rephaeli, Y., and Mather, J.C. 1990, ApJ, 350, 104
Fabian, A.C., Arnaud, K.A., Bautz, M.W., and Tawara, Y. 1994, ApJ, 436, L63
Fabian, A.C., Nulsen, P.E.J., and Canizares, C.R. 1991, Astron. Astrophys. Rev., 2, 191
Fukazawa, Y., Ohashi, T., Fabian, A.C., Canizares, C.R., Ikebe, Y., Makishima, K., Johnstone, R.M., and Fabian, A.C. 1995, MNRAS, 273, 625
Hurwitz, M., et al. 1998, ApJ, 500, L61.
Hu, E.M. 1992, ApJ, 391, 608
Knezek, P.M. and Bregman, J.N. 1998, AJ, 115, 1737
Koekemoer, A.M., O'Dea, D.P., Baum, S.A., Sarazin, C.L., Owen, F.N., and Ledlow, M.J. 1998, ApJ, 508, 608
Maoz, D. 1995, ApJ, 455, L115
McNamara, B.R., Bregman, J.N., and O'Connell, R.W. 1990, ApJ, 360, 20
McNamara, B.R., and Jaffe, W. 1994, A&A, 281, 673
O'Dea, C.P., Baum, S.A., and Gallimore, J.F. 1994, ApJ, 436, 669
O'Dea, C.P., Baum, S.A., Maloney, P.R., Tacconi, L.J., and Sparks, W.B. 1994, ApJ, 422, 467
O'Dea, C.P., Gallimore, J.F., and Baum, S.A. 1995, AJ, 109, 1669
O'Dea, C.P., Payne, H.E., and Kocevski, D. 1998, AJ, 116, 623
Schneider, D. P., et al. 1993, ApJS, 87, 45
Stickel, M., Lemke, D., Mattila, K., Haikala, L.K., and Haas, M. 1998, Ann. d'Astrophys., 329, 55
Voit, G.M. and Donahue, M. 1995, ApJ, 452, 162
White, D.A., Fabian, A.C., Johnstone, R.M., Mushotzky, R.F., and Arnaud, K.A. 1991, MNRAS, 252, 72



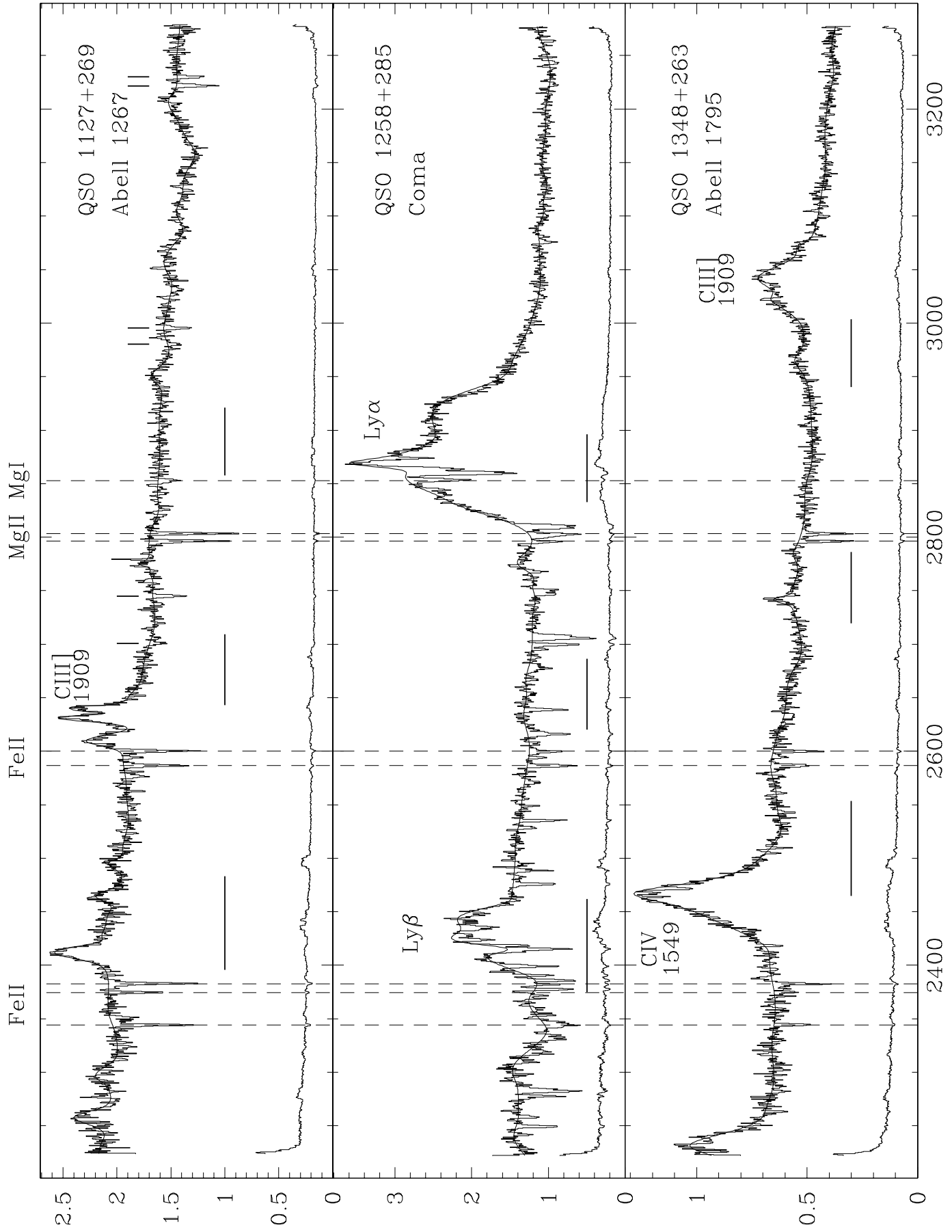


TABLE 1

QSO	z_{qso}	t_{exp} (s)	Date Obs.	Cluster	z_{cluster}	$\frac{d_{\text{proj}}}{R_{\text{cluster}}}$	R_{cluster} (Mpc)	\dot{M} $\frac{M_{\odot}}{\text{yr}}$
0020+287	0.51	7820	17 Nov 1996	Abell 21	0.0948	0.19	2.65	0
0107-156	0.861	3970	27 Jul 1996	Abell 151	0.0526	0.40	2.30	-
0909-095	0.63	8740	11 Feb 1997	Abell 754	0.0528	0.31	2.58	24
1127+269	0.378	4050	28 Nov 1996	Abell 1267	0.0321	0.19	1.68	-
1258+285	1.36	2100	5 Apr 1995	Abell 1656	0.0232	0.35	2.30	0
1348+263	0.59	6410	22 Jan 1997	Abell 1795	0.0616	0.72	1.94	295

TABLE 2

λ_{obs} (Å)	W_{λ} (Å)	FWHM (Å)	ID	v or z
QSO 0020+287				
2345.00 \pm 0.06	1.51 \pm 0.06	3.09 \pm 0.15	CIV 1548.19 (QSO)	0.515
2350.01 \pm 0.14	0.48 \pm 0.07	2.16 \pm 0.36	CIV 1550.77 (QSO)	0.515
2353.78 \pm 0.31	0.34 \pm 0.08	2.70 \pm 0.81
2375.10 \pm 0.22	1.18 \pm 0.12	4.50 \pm 0.54	FeII 2374.46 (MW)	80.29
2382.88 \pm 0.09	0.95 \pm 0.08	2.05 \pm 0.21	FeII 2382.76 (MW)	14.01
2578.39 \pm 0.40	0.50 \pm 0.13	3.10 \pm 0.95
2586.48 \pm 0.27	1.10 \pm 0.15	4.05 \pm 0.63	FeII 2586.65 (MW)	-20.00
2600.13 \pm 0.11	0.95 \pm 0.10	2.19 \pm 0.27	FeII 2600.17 (MW)	-4.61
2796.28 \pm 0.06	1.41 \pm 0.09	2.07 \pm 0.15	MgII 2796.35 (MW)	-8.20
2803.57 \pm 0.07	1.40 \pm 0.09	2.21 \pm 0.17	MgII 2803.53 (MW)	4.58
2815.76 \pm 0.35	0.27 \pm 0.08	2.04 \pm 0.00
2853.49 \pm 0.15	0.61 \pm 0.07	2.04 \pm 0.00	MgI 2852.96 (MW)	55.01
3011.57 \pm 0.30	0.46 \pm 0.12	2.43 \pm 0.72
QSO 0107-156				
2244.79 \pm 0.07	0.98 \pm 0.06	2.14 \pm 0.16	HI 1215.67 (QSO)	0.847
2257.28 \pm 0.28	0.19 \pm 0.04	2.02 \pm 0.00
2263.05 \pm 0.47	0.32 \pm 0.08	3.99 \pm 1.14
2268.67 \pm 0.26	0.25 \pm 0.05	2.02 \pm 0.00
2344.14 \pm 0.42	0.53 \pm 0.13	3.62 \pm 1.02	FeII 2344.21 (MW)	-10.04
2382.83 \pm 0.17	0.95 \pm 0.12	2.83 \pm 0.42	FeII 2382.76 (MW)	7.75
2397.53 \pm 0.11	0.94 \pm 0.10	2.16 \pm 0.27	CIV 1548.20	0.549
2402.00 \pm 0.15	0.62 \pm 0.08	2.02 \pm 0.00	CIV 1550.77	0.549
2577.41 \pm 0.34	0.24 \pm 0.07	2.04 \pm 0.00	MnII 2576.88 (MW)	62.07
2600.01 \pm 0.22	1.14 \pm 0.11	4.63 \pm 0.55	FeII 2600.17 (MW)	-18.66
2607.00 \pm 0.43	0.36 \pm 0.10	3.29 \pm 1.04	MnII 2606.46 (MW)	61.94
2778.91 \pm 0.37	0.23 \pm 0.07	2.04 \pm 0.00
2796.35 \pm 0.14	0.95 \pm 0.10	2.88 \pm 0.35	MgII 2796.35 (MW)	-0.25
2803.60 \pm 0.20	0.89 \pm 0.11	3.43 \pm 0.48	MgII 2803.53 (MW)	7.61
2884.86 \pm 0.29	0.26 \pm 0.06	2.04 \pm 0.00
3190.84 \pm 0.36	0.25 \pm 0.07	2.04 \pm 0.00
QSO 0909-095				
2286.25 \pm 0.37	0.39 \pm 0.11	2.60 \pm 0.89
2314.85 \pm 0.37	0.30 \pm 0.09	2.02 \pm 0.00
2344.14 \pm 0.15	0.77 \pm 0.11	2.17 \pm 0.36	FeII 2344.21 (MW)	-9.23
2374.19 \pm 0.30	0.72 \pm 0.14	3.29 \pm 0.72	FeII 2374.46 (MW)	-34.20
2382.72 \pm 0.17	1.01 \pm 0.12	2.94 \pm 0.41	FeII 2382.76 (MW)	-5.05
2489.35 \pm 0.32	0.31 \pm 0.09	2.38 \pm 0.77
2523.34 \pm 0.09	0.67 \pm 0.05	2.44 \pm 0.22	CIV 1548.19 (QSO)	0.630
2527.91 \pm 0.09	0.56 \pm 0.04	2.02 \pm 0.00	CIV 1550.77 (QSO)	0.630
2586.57 \pm 0.10	0.76 \pm 0.06	2.02 \pm 0.00	FeII 2586.65 (MW)	-9.90
2599.98 \pm 0.10	0.80 \pm 0.06	2.02 \pm 0.00	FeII 2600.17 (MW)	-22.62
2796.46 \pm 0.07	1.25 \pm 0.08	2.25 \pm 0.18	MgII 2796.35 (MW)	11.97
2803.62 \pm 0.07	1.17 \pm 0.08	2.17 \pm 0.18	MgII 2803.53 (MW)	9.44
2852.93 \pm 0.29	0.37 \pm 0.09	2.34 \pm 0.69	MgI 2852.96 (MW)	-3.23
3086.73 \pm 0.34	0.21 \pm 0.06	2.04 \pm 0.00

TABLE 2 (CONT.)

λ_{obs} (Å)	W_{λ} (Å)	FWHM (Å)	ID	v or z
QSO 1127+269				
2252.05 \pm 0.62	0.35 \pm 0.10	4.45 \pm 1.49
2344.13 \pm 0.07	0.85 \pm 0.06	2.12 \pm 0.17	FeII 2344.21 (MW)	-11.16
2374.52 \pm 0.12	0.51 \pm 0.04	2.04 \pm 0.00	FeII 2374.46 (MW)	7.22
2382.90 \pm 0.07	0.88 \pm 0.06	2.17 \pm 0.16	FeII 2382.76 (MW)	16.49
2576.67 \pm 0.28	0.30 \pm 0.06	2.77 \pm 0.66	MnII 2576.88 (MW)	-23.68
2586.55 \pm 0.08	0.76 \pm 0.05	2.25 \pm 0.18	FeII 2586.65 (MW)	-11.09
2594.18 \pm 0.25	0.21 \pm 0.04	2.04 \pm 0.00	MnII 2594.50 (MW)	-37.41
2600.29 \pm 0.05	0.88 \pm 0.05	2.12 \pm 0.13	FeII 2600.17 (MW)	13.76
2606.33 \pm 0.29	0.16 \pm 0.04	2.04 \pm 0.00	MnII 2606.46 (MW)	-14.71
2629.14 \pm 0.32	0.20 \pm 0.05	2.63 \pm 0.77
2700.85 \pm 0.30	0.21 \pm 0.06	2.35 \pm 0.70	FeII 2344.21	0.152
2744.96 \pm 0.12	0.45 \pm 0.05	2.12 \pm 0.28	FeII 2382.76	0.152
2796.32 \pm 0.05	0.98 \pm 0.04	2.04 \pm 0.00	MgII 2796.35 (MW)	-3.50
2803.49 \pm 0.05	1.06 \pm 0.03	2.04 \pm 0.00	MgII 2803.53 (MW)	-4.36
2852.72 \pm 0.23	0.36 \pm 0.06	2.78 \pm 0.54	MgI 2852.96 (MW)	-25.16
2980.19 \pm 0.32	0.20 \pm 0.06	2.33 \pm 0.77	FeII 2586.65	0.152
2995.51 \pm 0.15	0.39 \pm 0.05	2.21 \pm 0.35	FeII 2600.17	0.152
3031.19 \pm 0.62	0.29 \pm 0.08	4.50 \pm 1.48
3204.64 \pm 0.36	0.15 \pm 0.04	2.04 \pm 0.00
3221.81 \pm 0.09	0.63 \pm 0.06	2.22 \pm 0.22	MgII 2796.35	0.152
3230.12 \pm 0.13	0.41 \pm 0.04	2.04 \pm 0.00	MgII 2803.53	0.152
3273.44 \pm 0.61	0.39 \pm 0.11	4.28 \pm 1.44
QSO 1258+285				
2249.92 \pm 0.12	0.95 \pm 0.11	2.19 \pm 0.30	Ly β	1.194
2258.94 \pm 0.29	0.40 \pm 0.09	2.04 \pm 0.00	Ly β	1.203
2278.16 \pm 0.14	0.86 \pm 0.09	2.02 \pm 0.00	Ly β	1.222
2283.26 \pm 0.11	2.08 \pm 0.14	3.46 \pm 0.28	Ly β	1.227
2310.31 \pm 0.32	0.49 \pm 0.12	2.64 \pm 0.75	Ly α	0.900
2319.17 \pm 0.37	1.07 \pm 0.17	4.72 \pm 0.91	Ly β	1.262
2332.41 \pm 0.34	1.04 \pm 0.17	4.28 \pm 0.82	Ly α	0.918
2344.99 \pm 0.20	1.92 \pm 0.17	4.73 \pm 0.49	FeII 2344.21 (MW)	98.66
2354.03 \pm 0.33	0.35 \pm 0.09	2.02 \pm 0.00	Ly α	0.936
2372.10 \pm 0.36	0.31 \pm 0.09	2.02 \pm 0.00	FeII 2374.46 (MW)	-298.58
2378.09 \pm 0.12	0.84 \pm 0.07	2.02 \pm 0.00	Ly α	0.956
2382.73 \pm 0.23	0.47 \pm 0.08	2.02 \pm 0.00	FeII 2382.76 (MW)	-4.74
2386.39 \pm 0.10	0.97 \pm 0.07	2.02 \pm 0.00	Ly α	0.963
2391.17 \pm 0.21	0.47 \pm 0.08	2.02 \pm 0.00	Ly α	0.967
2399.68 \pm 0.08	1.05 \pm 0.08	2.17 \pm 0.20	Ly β	1.340
2415.73 \pm 0.07	1.36 \pm 0.09	2.32 \pm 0.18	Ly β	1.356
2419.14 \pm 0.13	0.64 \pm 0.06	2.02 \pm 0.00	Ly β	1.359
2424.40 \pm 0.16	0.54 \pm 0.10	2.04 \pm 0.38	Ly β	1.364
2435.65 \pm 0.27	0.88 \pm 0.13	3.94 \pm 0.68	Ly α	1.003
2447.94 \pm 0.38	0.46 \pm 0.10	3.39 \pm 0.90	Ly α	1.013
2476.42 \pm 0.09	0.98 \pm 0.09	2.26 \pm 0.23	Ly α	1.037
2488.99 \pm 0.14	0.64 \pm 0.07	2.04 \pm 0.00	Ly α	1.047
2529.08 \pm 0.22	0.39 \pm 0.07	2.04 \pm 0.00	Ly α	1.080
2535.87 \pm 0.10	0.91 \pm 0.06	2.04 \pm 0.00	Ly α	1.086
2571.31 \pm 0.36	0.52 \pm 0.11	3.41 \pm 0.86	Ly α	1.115
2586.93 \pm 0.07	1.21 \pm 0.08	2.16 \pm 0.17	FeII 2586.65 (MW)	32.39
2594.62 \pm 0.22	0.38 \pm 0.07	2.04 \pm 0.00	MnII 2594.50 (MW)	14.27
2600.20 \pm 0.13	0.96 \pm 0.10	2.73 \pm 0.32	FeII 2600.17 (MW)	2.84
2616.63 \pm 0.11	1.33 \pm 0.10	3.17 \pm 0.27	Ly α	1.152
2639.34 \pm 0.09	1.00 \pm 0.09	2.26 \pm 0.23	Ly α	1.171
2667.22 \pm 0.32	0.26 \pm 0.07	2.04 \pm 0.00	Ly α	1.194
2678.21 \pm 0.39	1.08 \pm 0.15	5.82 \pm 0.93	Ly α	1.203
2695.68 \pm 0.23	0.38 \pm 0.07	2.02 \pm 0.00	Ly α	1.217

TABLE 2 (CONT.)

λ_{obs} (Å)	W_{λ} (Å)	FWHM (Å)	ID	v or z
QSO 1258+285 (cont.)				
2700.10 ± 0.07	1.26 ± 0.08	2.25 ± 0.17	Ly α	1.221
2706.63 ± 0.07	2.86 ± 0.10	4.25 ± 0.19	Ly α	1.226
2748.49 ± 0.22	1.37 ± 0.13	2.50 ± 0.54	Ly α	1.261
2768.53 ± 0.21	0.40 ± 0.06	2.04 ± 0.00	Ly α	1.277
2796.40 ± 0.12	0.69 ± 0.06	2.04 ± 0.00	MgII 2796.35 (MW)	5.31
2802.91 ± 0.09	1.91 ± 0.10	3.50 ± 0.21	MgII 2803.53 (MW)	-66.79
2810.36 ± 0.08	2.62 ± 0.10	4.34 ± 0.20	Ly α	1.311
2821.57 ± 0.37	0.18 ± 0.06	2.04 ± 0.00	Ly α	1.321
2843.77 ± 0.60	0.57 ± 0.11	6.47 ± 1.45	Ly α	1.339
2854.02 ± 0.10	0.89 ± 0.06	2.85 ± 0.23	MgI 2852.96 (MW)	111.40
2860.39 ± 0.09	1.85 ± 0.11	3.42 ± 0.21	Ly α	1.352
2864.76 ± 0.17	1.00 ± 0.11	3.38 ± 0.41	Ly α	1.356
2874.02 ± 0.15	0.66 ± 0.07	3.07 ± 0.35	Ly α	1.364
3076.39 ± 0.22	0.43 ± 0.09	2.14 ± 0.51
QSO 1348+263				
2344.48 ± 0.15	0.62 ± 0.09	2.19 ± 0.37	FeII 2344.21 (MW)	33.94
2375.97 ± 0.76	0.82 ± 0.18	7.45 ± 1.94	FeII 2374.46 (MW)	191.02
2382.71 ± 0.09	0.83 ± 0.07	2.02 ± 0.00	FeII 2382.76 (MW)	-6.67
2418.64 ± 0.39	0.20 ± 0.06	2.04 ± 0.00
2432.60 ± 0.56	0.39 ± 0.12	3.85 ± 1.32
2543.10 ± 0.34	0.23 ± 0.06	2.04 ± 0.00
2586.62 ± 0.16	0.93 ± 0.09	3.35 ± 0.38	FeII 2586.65 (MW)	-3.20
2594.99 ± 0.37	0.28 ± 0.08	2.65 ± 0.88	MnII 2594.50 (MW)	56.73
2600.16 ± 0.09	0.75 ± 0.05	2.02 ± 0.00	FeII 2600.17 (MW)	-1.91
2632.52 ± 0.59	0.41 ± 0.11	4.60 ± 1.41
2745.79 ± 0.37	0.19 ± 0.06	2.04 ± 0.00
2796.45 ± 0.07	1.02 ± 0.05	2.04 ± 0.00	MgII 2796.35 (MW)	10.93
2803.41 ± 0.07	1.06 ± 0.07	2.27 ± 0.18	MgII 2803.53 (MW)	-12.67
3035.90 ± 0.63	0.37 ± 0.10	4.80 ± 1.50
3100.18 ± 0.33	0.25 ± 0.06	2.04 ± 0.00

TABLE 3

			$\log N_{\text{lim}} (\text{cm}^{-2})$					
Species	λ (Å)	f	A 21	A 151	A 754	A 1267	A 1656	A 1795
AlI	2264.16	0.133	13.08	13.08	13.13	12.69	13.19	13.10
CaI	2151.47	0.020	13.68	13.64	13.68	13.56	14.12	13.61
FeII	2382.77	0.343	12.64	12.62	12.53	12.41	12.94	12.51
MgI	2852.96	1.730	11.83	11.75	11.76	11.53	12.83	11.63
MgII	2796.35	0.629	12.28	12.18	12.21	11.99	12.51	12.11
MnII	2576.88	0.351	12.43	12.40	12.38	12.19	12.40	12.30
NaI	2853.72	0.002	14.96	14.90	14.89	14.68	14.89	14.83
SiI	2515.07	0.236	12.87	12.82	12.85	12.65	13.46	12.78

Figure 1. Calibrated HST/FOS spectra of six QSOs projected behind clusters. Axes are flux in units of 10^{15} ergs/s/cm²/Å vs. wavelength in Å. The upper line traces the QSO “continuum” fit, while the lower line shows the 3-sigma error spectrum which is propagated through the HST reduction pipeline along with the science data. QSO emission lines are identified, and strong Galactic absorption lines are denoted with dotted lines. Tick marks denote special absorption features discussed in the text. Regions marked with a bold line are locations we expect to see absorption from FeII or MgII in the cluster.

Table 1. Summary of the six observations and cluster/QSO characteristics. Five of the spectra were observed for this program; data for Coma were obtained from the HST archive. \dot{M} is the cooling rate; it is zero for non-cooling flow clusters.

Table 2. All detected lines, showing line center, equivalent width, probable ID, and velocity in km s⁻¹ (for Galactic components, identified as “MW”) or redshift (if of extragalactic origin). Uncertainties reported are 1- σ errors.

Table 3. Upper limits to the column densities of various species along each cluster line of sight. Also listed is the strongest transition for each species in the observed wavelength range, along with its f -value. The FeII and MgII transitions are the strongest lines expected from low-ionization absorbing gas.